

# Metallogenesis of the Baidi Au-Sb deposit, southwest Guizhou Province, China: mineralogical and geochemical evidence from sulfur-bearing minerals

Jun Yan<sup>1,2</sup>  · Yong Xia<sup>1</sup> · Qinqing Tan<sup>1</sup> · Zhuojun Xie<sup>1</sup> · Guosong Ji<sup>3</sup>

Received: 15 September 2023 / Revised: 22 October 2023 / Accepted: 28 October 2023 / Published online: 12 December 2023

© The Author(s), under exclusive licence to Science Press and Institute of Geochemistry, CAS and Springer-Verlag GmbH Germany, part of Springer Nature 2023

**Abstract** The Baidi Au-Sb deposit, which contains 8 t of Au and 10,979 Mt of Sb, is a typical and rare paragenetic deposit located in southwestern Guizhou Province, China. Previous studies have focused on individual ores, but have not combined them to identify their paragenetic mechanism or metallogenic regularity. Therefore, we used field investigations, microscopic observations, and in situ analyses to identify the spatial distribution, mineral paragenesis, compositional evolution, and metallogenic material sources of the ore bodies. We also determined the Au and Sb paragenetic characteristics and the metallogenesis of the deposit. The main Au-bearing minerals in the deposit were early (Apy1–2) and late (Apy3) stage arsenopyrites, as well as pre-mineralization (Py1), mineralization (Py2–5), and late mineralization (Py6–7) stage pyrites. The main Sb-bearing minerals were stibnite (Snt), skinnerite, bournonite, and valentinite. The minerals formed in the order of Py1, Py2–3 + Apy1, Py4–5 + Apy2, Snt, and Py6–7 + Apy3. The  $\delta^{34}\text{S}$  values of the arsenopyrites and pyrites ranged from  $-5$  to  $5\text{‰}$ , while those of stibnite were mostly less than  $-5\text{‰}$  in the later mineralization stages. Sulfur was provided by deep magmatic hydrothermal fluids, but

sedimentary sulfur was added in the later stages. Moreover, the trace elemental contents fluctuated and eventually became similar to those of the sedimentary strata. By comprehensively considering the ores along with the geological characteristics of the deposit, we determined that deep magma provided the Au during ore formation. Later tectonic changes provided Sb from the sedimentary strata, which precipitated along fault expansion areas and produced Au and Sb paragenesis.

**Keywords** Au-Sb mineralization · Arsenopyrite · Pyrite · Stibnite · Metallogenic process

## 1 Introduction

The Baidi Au-Sb deposit is located in Ceheng County, southwest Guizhou Province, China, and was initially studied as an important Sb ore resource in the 1970s. Subsequently, following the discovery of micro-disseminated Au deposits (i.e., Carlin-type Au deposits), the Baidi deposit was identified as a typical Au-Sb paragenetic deposit. Southwestern Guizhou Province is an important part of the Yunnan–Guizhou–Guangxi “Gold Triangle,” which contains the second-largest concentration of Carlin-type Au deposits in the world. It is also the core region of the South China low-temperature metallogenic domain (Hu et al. 2016), which is characterized by low-temperature mineral (Sb, Hg, Tl, As, Carlin-type Au, and Pb–Zn) deposits. The metallogenic characteristics of this area indicate that one of these elements is the main enriched and mineralized element, while the others are only associated and not mineralized. Spatially, the minerals are interspersed or underwent independent mineralization processes

✉ Yong Xia  
xiayong@vip.gyig.ac.cn

✉ Qinqing Tan  
tanqinqing@vip.gyig.ac.cn

<sup>1</sup> State Key Laboratory of Ore Deposit Geochemistry, Institute of Geochemistry, Chinese Academy of Sciences, Guiyang 550081, China

<sup>2</sup> Guizhou Institute of Technology, Guiyang 550003, China

<sup>3</sup> No.102 Geological Team, Guizhou Bureau of Geology and Mineral Exploration & Development, Zunyi 563003, China

(Liu et al. 2006; Hu et al. 2016; Hou et al. 2016) (Fig. 1). Therefore, the Baidi deposit is a typical Au-Sb paragenetic deposit in southwestern Guizhou Province (8 t of Au and 10,979 Mt of Sb resources) and understanding its paragenetic mechanism and metallogenic regularity are crucial for understanding low-temperature mineralization and

comprehensive mineral utilization in southwestern Guizhou Province.

The Baidi Au-Sb deposit is one of the earliest deposits in the Au concentration area of southwestern Guizhou Province. Previous studies have been conducted to investigate the geological background of the deposit, as well as for prospecting and exploration; however, these studies mostly

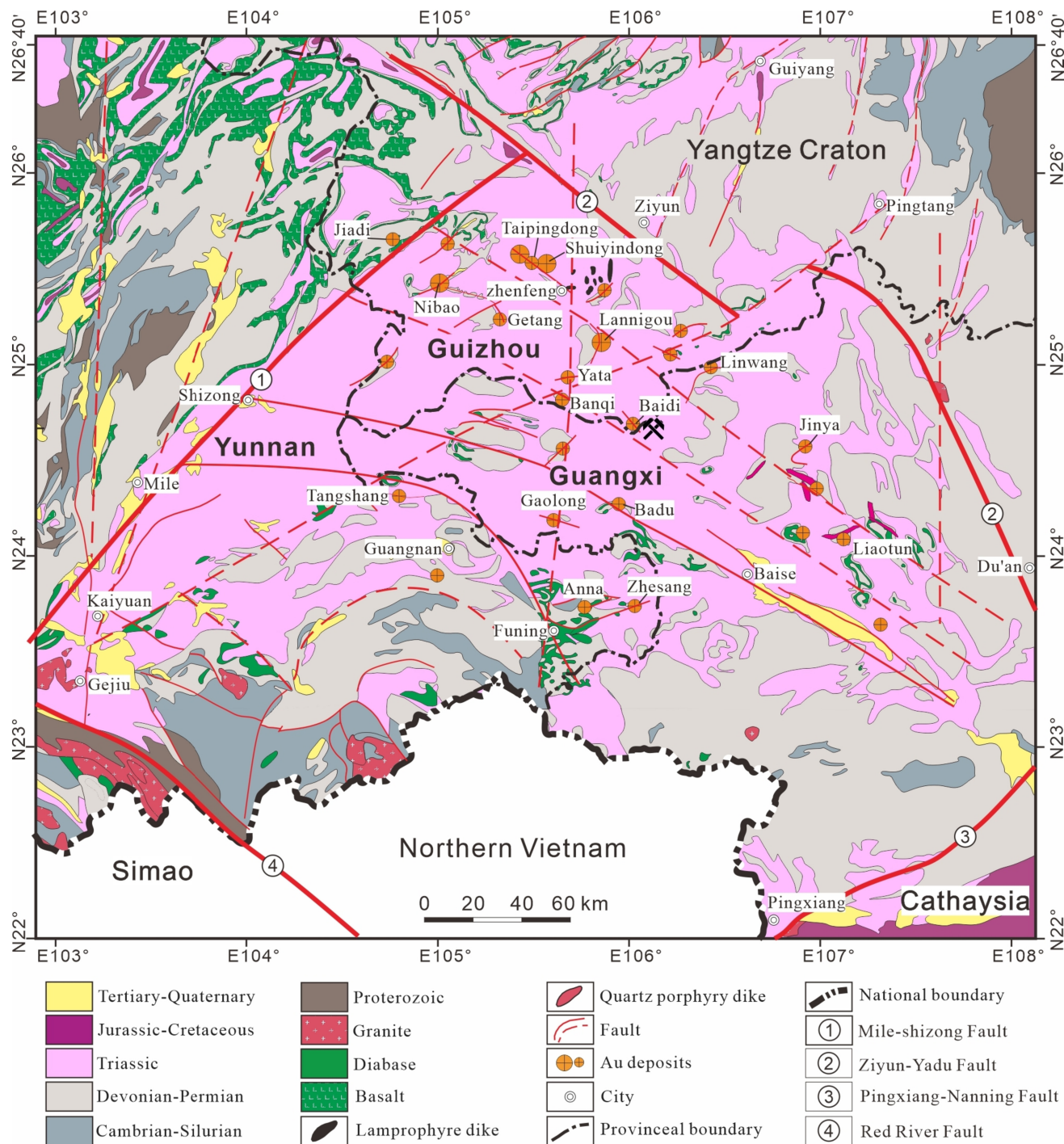


**Fig. 1** Distribution of mineral resources in southwestern Guizhou Province (Su et al. 2018; Tan et al. 2015)

concentrated on a single mineral of interest (Zhu 2009; Fang et al. 2013; Ji 2014; Ji et al. 2018; Wu et al. 2020). In addition, owing to the complex structure of the mining area, research and exploration have proceeded slowly. Thus, the spatial and genetic characteristics of the Au–Sb paragenetic deposits in the region have not yet been identified.

Therefore, based on previous studies, we explored the regional characteristics of the Baidi deposit and the spatial distribution of ore bodies using field investigations. We also identified the main mineral paragenetic characteristics and elemental occurrences using polarized light microscopy and scanning electron microscopy (SEM). In situ inductively coupled plasma mass spectrometry (ICP-MS) was used to measure the trace elemental and sulfur isotopic contents of the major metal sulfides (i.e., pyrite, arsenopyrite, and stibnite), determine the fluid compositional evolution and the ore-forming material source, and provide a basis for an improved understanding of the ore-forming process.

## 2 Regional geology

The Yunnan–Guizhou–Guangxi region is located in the Youjiang Basin on the southwestern margin of the Yangtze Plate (Fig. 1). This region contains various types of deposits, including Carlin-type Au deposits. The dominant minerals contain Au, Sb, Hg, and Tl (Hu et al. 2016). This region is also the main area of the South China low-temperature metallogenic domain (Zhou and Hu 1995; Li 1999; Hu et al. 2002; Tu 2002; Qiu et al. 2016). The formation and enrichment of “Gold Triangle” Carlin-type Au deposits were closely related to the evolution of the Youjiang Basin and have been investigated for more than 40 years (Xu 1987; Chen and Zeng 1990; Zhuang 1995; Yin et al. 1999; Wang et al. 2000; Jian et al. 2009; Du et al. 2013; Metcalfe 2013; Lehrmann et al. 1978; Yang et al. 2020). These deposits are also related to the evolution of the Paleo-Tethys Ocean in this region, which was characterized by a littoral and neritic sedimentary environment during the Early-Middle Devonian. At this time, the extensional environment underwent intensified late cracking, which resulted in the formation of alternating platforms and basins, in which the platforms were isolated carbonate deposits and the basins were deep water argillaceous rocks, sandstones, siltstones, or siliceous rocks. At the end of the Middle Permian, the platform shrank owing to the subduction of the Indosinian Plate, and the platform and basin pattern gradually disappeared, forming a foreland basin. From the Late Permian to the Early-Middle Triassic, magmatic activity produced the Emeishan basalt. In the Early-Middle Triassic, the Paleo-

Tethys Ocean was further subducted and many terrigenous clastic turbidites were deposited. In the Late Triassic, the basin was uplifted above sea level owing to the convergence of the Indosinian Plate and became a peripheral foreland basin. During the Middle Jurassic-Late Early Cretaceous, influenced by Paleo-Pacific Plate subduction beneath the Eurasian Plate, northeast-trending compressional tectonics were prominent and controlled magmatism, which was characterized by basic diabase intrusions in the Jurassic. In the Late Early Cretaceous, alkaline ultrabasic rock assemblages formed, reflecting the extensional environment during this period.

The evolution of the Youjiang Basin essentially reflects the formation and evolution of regional structures, sedimentary environments, and fluids, in which the regional structure determined fluid migration paths, heat distribution and diffusion, and ore body occurrence. The sedimentary environment determined the sedimentary associations: the ore-bearing lithology in the basin is mainly clastic rock, the platform is carbonate, and the platform margin is reef limestone. Fluid flow in the basin occurred in multiple phases. Although the source of the ore-forming fluids remains uncertain, the basin fluids did affect ore formation (Yang et al. 2020).

## 3 Deposit geology

The outcropping stratigraphy in the mining area is divided into two distinct sequences in deep-water basin terrigenous clastic rock of the Middle Triassic Xuman Formation and Quaternary system in the upper sequence. According to its lithology, thickness, and other characteristics, the Xuman Formation can be divided into four sections (from bottom to top): The Xuman Formation 1 ( $T_2xm^1$ ), which is not exposed in the mining area; The Xuman Formation 2–3 ( $T_2xm^{2-3}$ ), which are distributed in the central mining area and are the main Au- and Sb-bearing horizons characterized by interbedded thin–medium–thick fine-grained siltstones and thin clays with small amounts of micrite (total thickness of  $\sim 780$  m); and The Xuman Formation 4 ( $T_2xm^4$ ), which is distributed to the west and northeast of the mining area and is characterized by interbedded grey medium-thick fine-grained siltstones and grayish-green and dark grey thin–medium–thick claystone of unequal thicknesses greater than 300 m (Fig. 2) (Zhu 2009; Fang et al. 2013; Ji 2014; Ji et al. 2018; Wu et al. 2020).

The Baidi Au–Sb deposit is located in the northwestern part of the Youjiang Basin (Figs. 1, 2) and is controlled by the Qinglong–Ceheng deep fault. The distribution of the deposit is controlled by an arc-shaped complex fold and a secondary axial fault structure, as the deposit is located at the intersection of these two structures. The complex fold

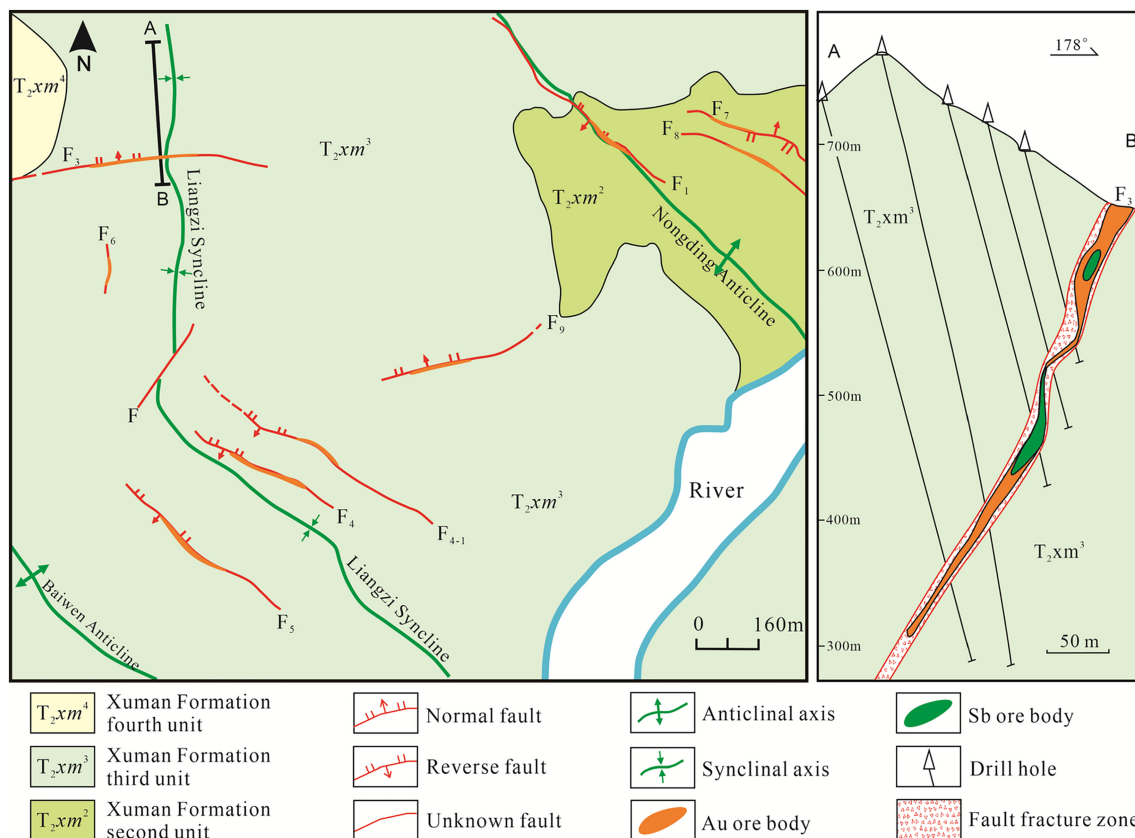


**Fig. 2** Structural geology and exploration profile of the Baidi Au-Sb deposit

is generally oriented northwest to southeast and comprises (from west to east) the Nongding anticline, Liangzi syncline, and Baiwen anticline. The folds are all parallel to each other and develop a series of secondary parallel folds to the south. Most of the fault structures in this area are high-angle compressional thrust faults that strike parallel to the fold axis (i.e., to the northwest), while some strike E–W and to the northeast (Zhu 2009; Fang et al. 2013; Ji 2014; Ji et al. 2018; Wu et al. 2020). To date, 8 Au and 11 Sb ore bodies have been identified in the Baidi Au-Sb deposit. The ore bodies are controlled by the fault structure, and most occur as lenticular bodies along fracture zones or joint fissures. The Au and Sb ore bodies are located close to the  $F_3$  and  $F_4$  faults, and the Sb ore bodies are often located in fault extension areas or locations with obvious changes in dip (Fig. 2). The Au ore bodies are 20–360 m long, with an average thickness of 1.63–5.61 m and an average grade of  $1.56\text{--}5.28 \times 10^{-6}$ . The Sb resources are close to medium scale, with lengths of 20–240 m, an average thickness of 0.65–12.69 m and an average grade of 1.42–11.15 % (Wu et al. 2020).

Alteration types observed in the Baidi deposit include silicification, pyritization, arsenopyritization, stibnite mineralization, carbonatization, and clayization. The metallic minerals include arsenopyrite, pyrite, and stibnite, while

the non-metallic minerals include quartz, clay minerals, dolomite, muscovite, calcite, and carbonaceous minerals. The ore structures are mainly disseminated and brecciated, with some laminated stockworks and vein structures.

#### 4 Sampling and analytical methods

Seventeen samples were collected from the No. 3 ore body, which is controlled by Fault 3 (Fig. 2), which is one of the larger ore bodies in the Baidi Au-Sb deposit. Sampling site selection was mainly based on elevation and differences in the Au and Sb grades. Representative samples were selected and ground into polished thin sections, and mineral types and relationships were identified using polarized-light microscopy and SEM. Analytical points were selected based on the high-resolution SEM images, and the trace elemental and isotopic contents of arsenopyrite, pyrite, and stibnite were analyzed using ICP-MS.

Mineralogical analyses were performed at the Resource Exploration Engineering Laboratory of the Guizhou Institute of Technology (Guiyang, China) and Wuhan Shangpu Analytical Technology Co., Ltd (Wuhan, China). The polarizing microscope (Olympus BX51-P, Olympus, Tokyo, Japan) had a maximum magnification of  $10 \times 100$

(eyepiece  $\times$  objective). The SEM used for backscatter image analysis was a JSM-IT300 (JEOL, Tokyo, Japan). According to the characteristics of the samples, a high acceleration voltage of 20 kV was used and was increased incrementally. To ensure that the effect was not sustainable, the contrast and grayscale were adjusted appropriately. The image was focused until it did not move or only moved minimally. An IRA3-EDAX Element 30 (EDAX, Berwyn, PA, USA) was used for energy spectrum analysis. Prior to analysis, the surface of each sample was wiped with alcohol and a carbon coating was applied to eliminate surface charge effects. The acceleration voltage was 25 keV and X-ray acquisition was performed in spot mode. The analytical procedures and conditions are described in detail in Qi jingyu. (Qi 2006).

In situ trace elemental analyses of the sulfur-bearing minerals were performed at Beijing Zirconium Pilot Technology Co., Ltd (Beijing, China) using a PQMS Elite ICP-MS (Analytik, Jena, Germany) with a RESOLUTION 193 nm excimer laser ablation (LA) system (ASI, Fyshwick, Australia). The laser beam used for ablation had a diameter of 30  $\mu\text{m}$ , a frequency of 5 Hz, and an energy density of approximately 3 J/cm<sup>2</sup> in. High-purity He was used as the carrier gas. NIST 610 was used to tune the instrument to optimal conditions prior to analysis. The LA-ICP-MS sampling adopted a single-point ablation method. During analysis, the laser beam was first blocked for 20 s for blank background collection, after which the sample was continuously ablated for 45 s. After ablation, the sample injection system was purged for 20 s. The single-point testing and analysis time was 85 s. A set of NIST 610, NIST 612, BHVO-2G, BCR-2G, BIR-1G, and MASS-1 standards were analyzed after every 10 ablation points to quantitatively calculate their elemental contents.

Multi-collector ICP-MS (MC-ICP-MS sulfur isotope ratio analyses (Neptune Plus, Thermo Fisher Scientific, Waltham, MA, USA) used a beam spot size and laser ablation frequency of 16–100  $\mu\text{m}$  and 6–8 Hz, respectively, which were adjusted according to the S signal intensity of the samples. The laser energy density was 7.0–8.0 J/cm<sup>2</sup>. The Faraday cup simultaneously received <sup>32</sup>S and <sup>34</sup>S, and the integration time was 0.131 s. Two hundred sets of data were collected, and the total time for each sample analysis was  $\sim$  27 s. Prior to analysis, the instrumental parameters were adjusted using the standard sulfide samples Balmat FeS, MXG, and Balmat ZnS to achieve the best conditions. To reduce the influence of the matrix effect on the results, a sulfide similar to the sample matrix was used as a standard during analysis, and the standard–sample–standard cross method was used for mass discrimination corrections. Specific analytical and data processing methods are described in Pearce et al. (1997) and Liu et al. (2008).

## 5 Results

### 5.1 Petrographic characteristics of the main Au-and Sb-bearing minerals

The main Au-bearing minerals were arsenopyrite and pyrite. Based on the locations, shapes, structures, and chemical compositions of the minerals, the arsenopyrites were divided into two metallogenic stages and three generations, while the pyrites were divided into three metallogenic stages and seven generations.

During the metallogenic period, the crystal morphologies of arsenopyrite (Apy) were mostly rhombic, lance-shaped, needle-shaped, banded, and radial aggregates. Arsenopyrite, pyrite, and quartz formed paragenetic mineral assemblages during this period, which were divided into two generations according to their distributions and combined characteristics. Ore arsenopyrite 1 (Apy1) was the most common type and was distributed in the sandstones and mudstones in idiomorphic particles, banded and radial aggregates (Fig. 3A and B), or radial aggregates composed of pyrite (Fig. 3C). Particle sizes ranged from 0.01 to 0.1 mm. Ore arsenopyrite 2 (Apy2) filled quartz veins as an aggregate with particle sizes of 0.01–0.1 mm (Fig. 3D), and arsenopyrite particles encased in stibnite were occasionally observed (Fig. 3E). In the late mineralization stage, post-ore arsenopyrite 3 (Apy3) and pyrite formed aggregates in the carbonate veins (Fig. 3F).

Pre-metallogenic pyrite (Py) was characterized by strawberry-like aggregates of pre-ore pyrite 1 comprising fine euhedral grains, with an aggregate size of  $<$  30  $\mu\text{m}$  (most were  $\sim$  8  $\mu\text{m}$ ; Fig. 4A and B). During the mineralization period, pyrite exhibited hypidiomorphic–euhedral granular forms, and most samples exhibited obvious zonation. Pyrite formed a paragenetic mineral assemblage with arsenopyrite and quartz. According to the backscatter images, the assemblages were mainly composed of ore pyrite 2 with patchy distributions, ore pyrite 3 with high As contents, ore pyrite 4 with relatively high As contents, and thin layers of ore pyrite 5 (Fig. 4C and D). Most of the outer annuli comprised several secondary annuli with thicknesses of 3–5  $\mu\text{m}$ . The pyrite in the late mineralization stage formed irregularly shaped xenomorphic granules, and had low Au and high As contents. The pyrite, arsenopyrite, and carbonate veins from the stage formed a paragenetic mineral association with two notable layers of zonation. The inner zone of post-ore pyrite 6 was thicker, (mostly 100–300  $\mu\text{m}$ ), whereas the outer zone of post-ore pyrite 7 was narrower (15–30  $\mu\text{m}$ ) and was characterized by secondary zones (3–5  $\mu\text{m}$ ) (Fig. 4E and F).

According to hand specimen and microscopic observations, stibnite was the main Sb-bearing mineral in the

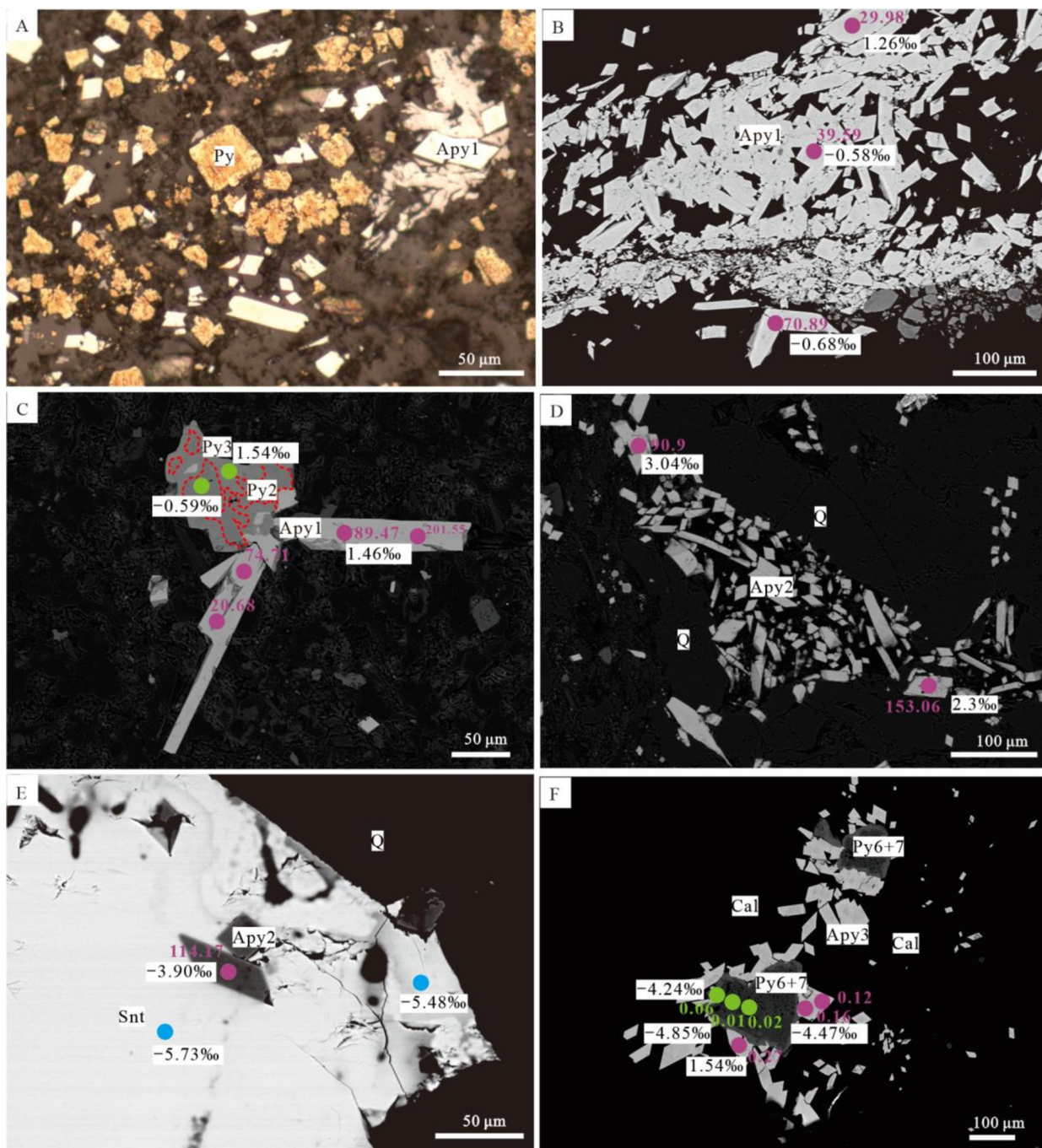


**Fig. 3** Different arsenopyrite types in the Baidi Au-Sb deposit **A** Idiomorphic granular pyrite and rhombohedral/columnar ore arsenopyrite 1 in sandstones and mudstones; **B** Banded ore arsenopyrite 1; **C** Radial ore arsenopyrite 1; **D** Ore arsenopyrite 2 in quartz veins; **E** Ore arsenopyrite 2 encased in stibnite and distributed in quartz veins; **F** Radial post-ore arsenopyrite 3 in calcite veins and aggregates formed with post-ore pyrite 6 + 7. Abbreviations: Py = pyrite, Apy1 = ore arsenopyrite 1, Py2 = ore pyrite 2, Py3 = ore pyrite 3, Apy2 = ore arsenopyrite 2, Q = quartz, Snt = stibnite, Py6 + 7 = post-ore pyrite 6 + 7

mining area, mainly occurring as euhedral crystals with tabular, flaky, short columnar, and needle-columnar forms. Stibnite filled rock fissures, ore fissures, and quartz vein miarolitic cavities in the tectonic alteration zone (Fig. 5A

and B). Moreover, according to the SEM analyses, a series of Pb-Sb sulfosalts (e.g., skinnerite, bournonite) and Sb blooms were also present (Fig. 5C–E).

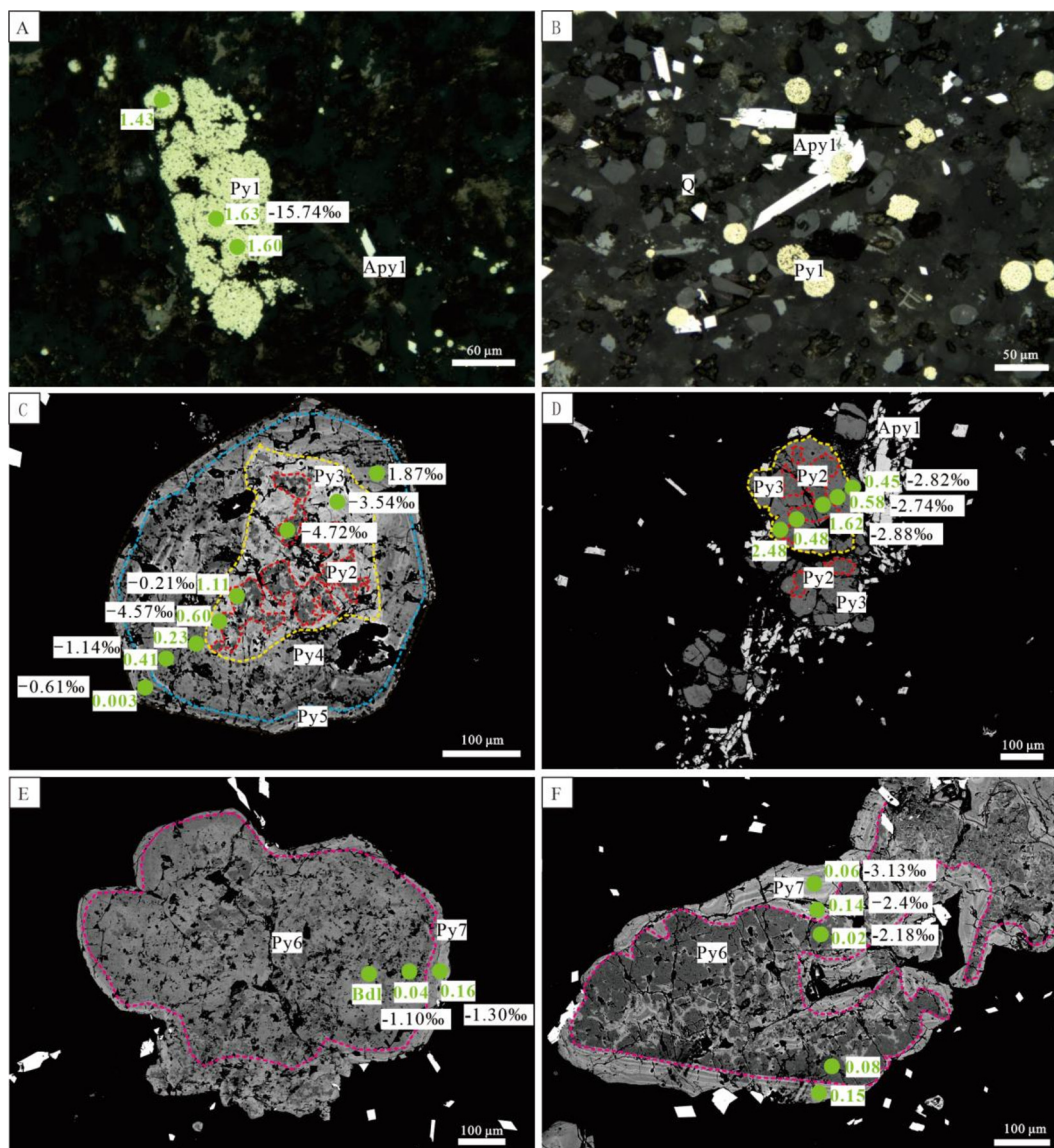


**Fig. 4** Different pyrite types in the Baidi Au-Sb deposit: **A** Strawberry-like pre-ore pyrite 1 aggregate; **B** Strawberry-like pre-ore pyrite 1 and radial ore arsenopyrite 1 forming an aggregate; **C** Pyrite distributed in the sandstones and mudstones during the hypidiomorphic–authigenic mineralization period, in which the dark ore pyrite 2 in the core is patchy and continuously advances toward the edge, followed by bright ore pyrite 3 with high As contents, relatively dark ore pyrite 4 with high As contents, and bright ore pyrite 5 with more outer secondary zones; **D** Aggregate of ore pyrite 2, ore pyrite 3, and ore arsenopyrite 1 tangential to a quartz vein; **E**, **F** Blocky pyrite distributed in calcite veins, comprising a dark inner post-ore pyrite 6 band and an outer polycyclic post-ore pyrite 7 band. Abbreviations: Apy1 = ore arsenopyrite 1, Py1 = pre-ore pyrite 1, Py2 = ore pyrite 2, Py3 = ore pyrite 3, Py4 = ore pyrite 4, Py5 = ore pyrite 5, Py6 = post-ore pyrite 6, Py7 = post-ore pyrite 7

## 5.2 Trace elemental compositions of arsenopyrite, pyrite, and stibnite

The results obtained from the trace elemental analyses of the arsenopyrite from different generations are shown in Online Appendix 1. The elemental characteristics of Apy1 distributed in the sandstones and mudstones differed from those of the other arsenopyrite generations. The average Au content of the rhombic, lance-shaped, and radial, arsenopyrites was 95.26 ppm, with a maximum content of

391.24 ppm, indicating that arsenopyrite was the main Au-bearing mineral (Figs. 3A, B, and 4A, D). Another type of arsenopyrite (Figs. 3C, 4B) that formed radial aggregates with pyrite had the same Au content (average of 91.74 ppm, maximum of 201.55 ppm) and exhibited an increasing trend from the center to the radial edge. The Co and Ni contents of the singular arsenopyrite crystals (34.48 and 215.62 ppm, respectively) were lower than those of arsenopyrite associated with pyrite (131.03 and 1143.52 ppm, respectively).

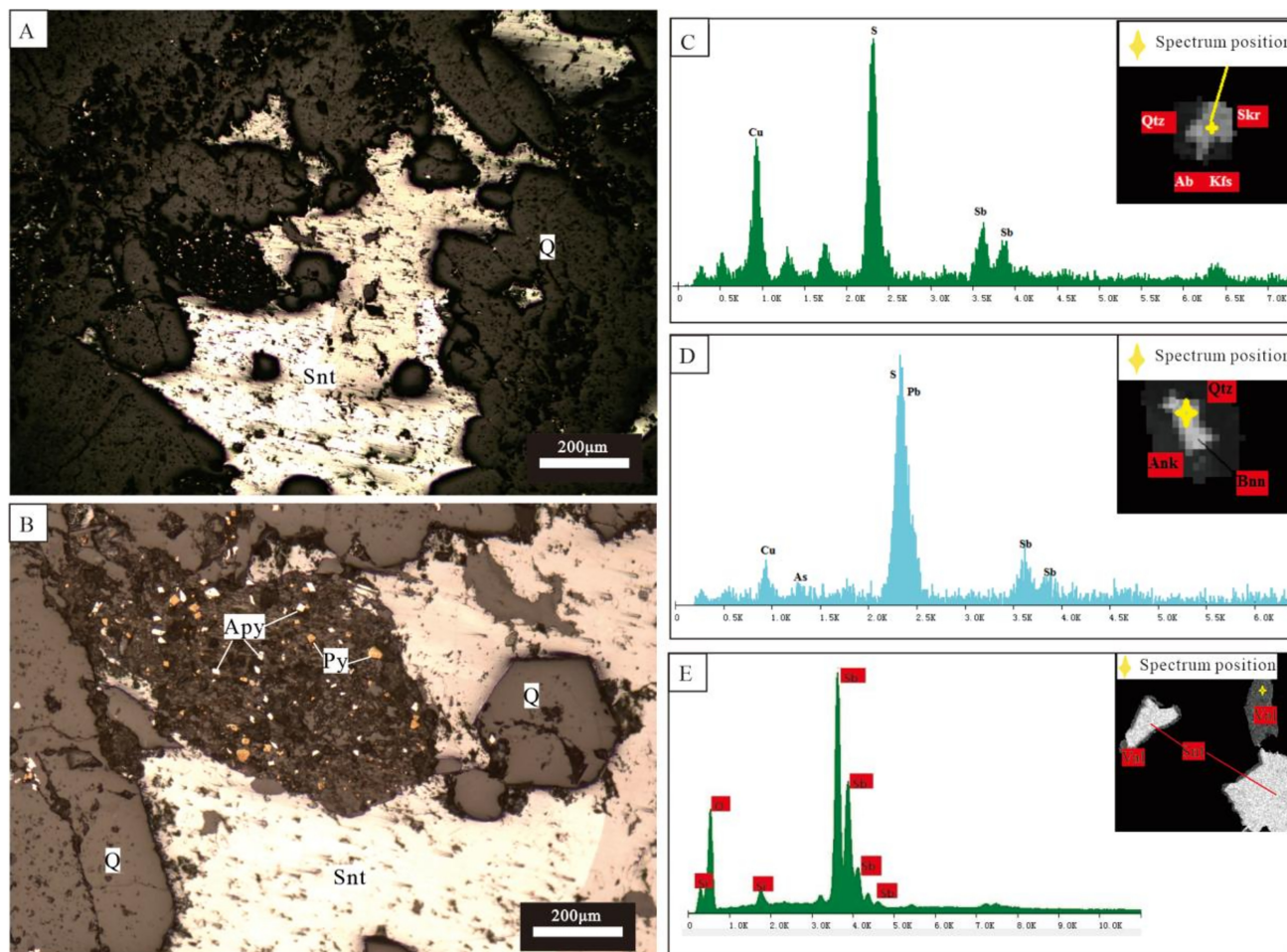


**Fig. 5** Sb-bearing minerals and their contents in the Baidi Au-Sb deposit: **A** Euhedral stibnite in quartz veins (reflected light F); **B** Euhedral stibnite (orthorhombic +) in quartz veins; **C** Backscatter image and energy spectrum of skinnerite; **D** Backscatter image and energy spectrum of bournonite; **E** Backscatter image and energy spectrum of valentinite (*Snt* Stibnite, *Q* Quartz, *Skr* Skinnerite, *Ab* Albite, *Kfs* K-feldspar, *Bnn* Bournonite, *Ank* Ankerite, *Val* valentinite)

The Apy2 filling the quartz veins was mainly rhombic and lance-shaped, with some crystals encased in stibnite within the quartz veins (Fig. 4E). The average Au content was 111.56 ppm and the maximum was 174.35 ppm. In addition, some rhombic arsenopyrite was encased in stibnite, with an average Au content of 114.17 ppm. Owing to the influence of stibnite, the Fe and As contents were low, with a higher Sb content (443464.96 ppm).

The Apy3 filling the carbonate veins was either radial, in aggregates with pyrite (Fig. 3F), or scattered in rhombic aggregates (Fig. 4E and F). The Au contents of Apy3 were generally low, with an average of 0.19 ppm and a maximum of 0.27 ppm. The major elemental contents of Apy3 were similar to those of Apy1.

The results obtained from the trace elemental analyses of the pyrite from different generations are shown in Online Appendix 1, and the mean and median elemental contents are shown in Table 1.

The strawberry-like Py1 aggregates (Fig. 4A and B) that formed in the early mineralization stage had Au contents of 1.43–1.63 ppm (average of 1.56 ppm) and were characterized by high As, Sb, Tl, Co, and Ni contents, with (average values of 23,419, 133.56, 2.75, 535.99, and 508.97 ppm, respectively). Compared with Py1, Py2, which exhibited a patchy distribution, had a similar Au content (0.06–1.62 ppm), higher As (13841–48029 ppm, average of 26253 ppm), and Sb (104.41–650 ppm, average of 287 ppm) contents, and a lower Tl content (0.04–1.17 ppm, average of 0.20 ppm). Compared with Py2, Py3 had higher Au (0.45–11.45 ppm, average of 2.2 ppm) and As (25353–91910 ppm, average of 38577.67 ppm) contents; however, the Sb and Tl contents were similar to those of Py2 (averages of 239.13 and 0.55 ppm, respectively). Py4 was characterized by low Au (0.23–0.41 ppm, average of 0.32 ppm) and As (14656–16256 ppm, average of 15456 ppm) contents. Py4

**Table 1** Average trace elemental contents of arsenopyrite, pyrite, and stibnite from the Baidi Au-Sb deposit ( $\mu\text{g/g}$ )

Mineral	Number	Au	As	Sb	Tl	Co	Ni	Cu	Pb	Ti	Zn	Sr
Apy1	$n = 20$	94.20	437,263.03	494.92	796.91	63.44	493.99	280.84	34.57	2016.56	23.19	27.37
Apy2	$n = 3$	110.69	453,970.89	413.94	0.20	40.25	193.09	173.92	28.71	9.73	8.60	3.24
Apy3	$n = 3$	0.19	404,052.79	2309.08	0.03	21.30	76.73	426.15	119.93	3.53	9.04	29.97
Py1	$n = 3$	1.56	23,418.62	133.56	2.95	535.99	508.97	269.31	66.15	2.95	7.75	4.83
Py2	$n = 11$	0.60	26,253.38	287.00	0.20	45.23	637.48	509.06	447.05	802.44	69.10	3.66
Py3	$n = 9$	2.01	37,405.08	237.31	0.50	12.71	58.71	444.27	109.87	239.59	61.45	7.68
Py4	$n = 2$	0.32	15,456.25	22.65	0.09	3.42	12.61	158.99	21.85	17.10	0.84	0.49
Py5	$n = 1$	0.00	16,055.38	5.51	0.02	2.19	9.74	129.94	7.92	130.90	0.64	3.74
Py6	$n = 15$	0.06	11,454.88	105.3	0.02	11.73	131.24	300.86	306.26	2.62	80.17	1.27
Py7	$n = 13$	0.06	19,329.52	76.5	0.02	10.21	75.43	317.3	81.86	1.58	41.31	1.38
Snt	$n = 2$	0.80	10.78	679,944.74	0.00	0.01	0.00	3.53	32.95	1.21	0.72	0.47

also exhibited low Sb and Tl contents (averages of 22.65 and 0.09 ppm, respectively). Py5 had low Au, As, Sb, and Tl contents (averages of 0.0034, 16055, 5.51, and 0.02 ppm, respectively). Overall, the Au contents of pyrite that formed during the mineralization period were above the detection line but were far lower than those measured in the arsenopyrite. Their As contents were generally high (minimum of 13,841 ppm), their Sb contents varied widely (5.51–650 ppm), and had low Tl contents that also varied widely (0.02–1.4 ppm).

In the late mineralization stage, Py6–7 (Fig. 4E and F) were mainly distributed in carbonate veins or veins composed of both quartz and carbonate. Py7 is brighter than Py6 and located in the outer band. The major elemental contents (i.e., Au, As, Sb, and Tl) were lower than those of the pyrite that formed in the mineralization stage. The Au contents were particularly low (0–0.2 ppm, average of 0.06 ppm). The As contents varied widely (1385–44605 ppm), with the outer band containing more As (average of 19329.52 ppm). The other elemental contents varied to some extent, but had similar average values of Py6 and Py7 (Table 1).

The contents of the major elements S and Sb were 99.97–99.99%, and the contents of other trace elements were relatively low. The Pb and Ti contents were relatively uniform (averages of 33 and 1.2 ppm, respectively). As was present in some locations (average of 21.55 ppm). In addition, Au was present near the arsenopyrite area (average of 1.59 ppm) (Table 1).

### 5.3 Sulfur isotopic characteristics of arsenopyrite, pyrite, and stibnite

The  $\delta^{34}\text{S}$  values of the arsenopyrite, pyrite, and stibnite were quantitatively analyzed using LA-MC-ICP-MS. The arsenopyrite and pyrite from all mineralization stages were

analyzed at 35 points to determine their zonal characteristics (Online Appendix 2). The data for arsenopyrite (i.e., the main Au-bearing mineral) indicate that Apy1 ( $n = 13$ ) had  $\delta^{34}\text{S}$  values ranging from  $-0.68$  to  $+3.73$  ‰, (median of 1.27 ‰), Apy2 ( $n = 7$ ) had  $\delta^{34}\text{S}$  values ranging from  $-3.9$  to  $+3.23$  ‰ (median of 2.3 ‰), and Apy3 ( $n = 1$ ) had an  $\delta^{34}\text{S}$  value of 1.54 ‰. For the pyrite, Py1 ( $n = 2$ ) had  $\delta^{34}\text{S}$  values ranging from  $-15.74$  to  $-5.5$  ‰ (average of  $-10.62$  ‰), Py2 ( $n = 7$ ) had  $\delta^{34}\text{S}$  values ranging from  $-2.88$  to 1.74 ‰ (median of  $-0.59$  ‰), Py3 ( $n = 7$ ) had  $\delta^{34}\text{S}$  values ranging from  $-4.57$  to 1.54 ‰ (median of  $-2.74$  ‰), Py4 ( $n = 4$ ) had  $\delta^{34}\text{S}$  values ranging from  $-1.86$  to 1.87 ‰ (average of  $-0.2$  ‰), and Py5 ( $n = 3$ ) had  $\delta^{34}\text{S}$  values ranging from  $-1.15$  to 2.07 ‰ (median of  $-0.61$  ‰). A total of 17 points were analyzed in pyrite from the late mineralization stage, for which the  $\delta^{34}\text{S}$  values ranged from  $-4.58$  to  $-1.1$  ‰ (median of  $-2.52$  ‰). Stibnite, (i.e., the main Sb-bearing mineral) was

**Table 2** Sulfur isotopic contents of sulfides in the Baidi Au-Sb deposit (‰)

Mineral	Max	Min	Median	Average
Apy1	3.73	$-0.68$	1.27	1.10
Apy2	3.23	$-3.90$	2.30	1.51
Apy3	1.54	1.54	1.54	1.54
Py1	$-5.5$	$-15.74$	$-10.62$	$-10.62$
Py2	1.74	$-2.88$	$-0.59$	$-0.85$
Py3	1.54	$-4.57$	$-2.74$	$-1.59$
Py4	1.87	$-1.86$	$-0.20$	$-0.20$
Py5	2.07	$-1.15$	$-0.61$	0.10
Py6	$-1.3$	$-4.24$	$-2.91$	$-2.74$
Py7	$-1.1$	$-4.85$	$-2.49$	$-2.60$
Snt	$-5.48$	$-5.73$	$-5.61$	$-5.61$

analyzed at 2 points, yielding an average  $\delta^{34}\text{S}$  of  $-5.61\text{‰}$  (Table 2).

## 6 Discussion

### 6.1 Sulfur sources

By analyzing the mineral paragenesis and elemental contents, we summarized and divided the main mineral assemblages and relationships into three stages: pre-mineralization (Py1), mineralization (Py2–5 and Apy1–2), and post-mineralization (Py6–7 and Apy3). Figure 6 shows the details of these stages.

Arsenopyrite was divided into ore arsenopyrite 1–2 (Apy1–2) and post-ore arsenopyrite 3 (Apy3) stages; pyrite was divided into pre-ore pyrite 1 (Py1), ore pyrite 2–5 (Py2–5), and post-pyrite 6–7 (Py6 + 7) stages; Sb-bearing minerals were the products of the late ore stage; quartz was widely distributed from the ore to the post-ore stage; and carbonate minerals formed in the post-ore stage.

The  $\delta^{34}\text{S}$  value of pyrite Py1 in the pre-ore stage varied widely (Table 2, Fig. 7), which is consistent with previous findings from fine-grained/strawberry-shaped pyrite in the early ore stages of other deposits in southwestern Guizhou Province (Guo 1988; Li et al. 1995; Hofstra and Cline 2000; Xia 2005; Zhang et al. 2008, 2010; Jin and Li 2017; Xie et al. 2018; Yan et al. 2018; Chen et al. 2021). However, compared with other deposits (e.g., Jinfeng, Yata, and Jinya) the pyrite  $\delta^{34}\text{S}$  values in the Baidi deposit during this period were relatively low, with negative values (minimum of  $-15.74$  and maximum of  $-5.5$ ). The

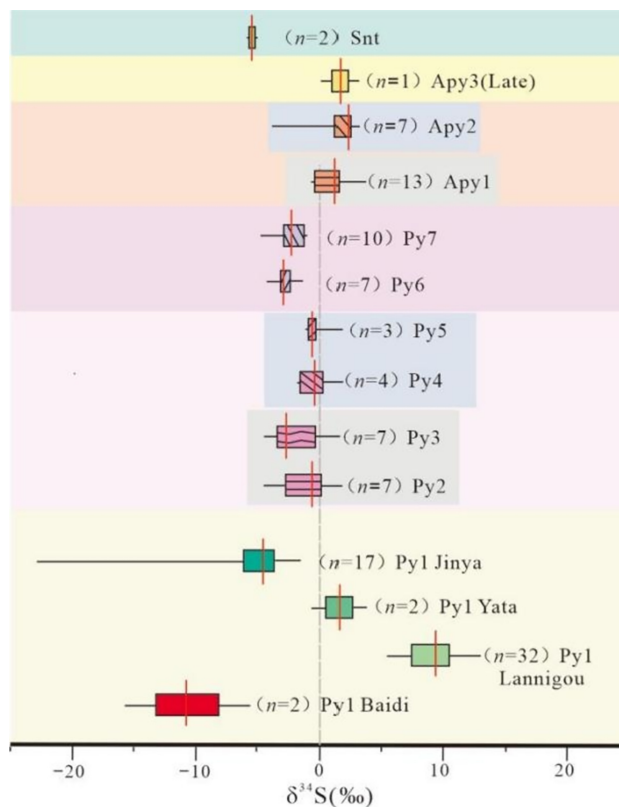


**Fig. 7** Box diagram of sulfur isotopic distributions in the Baidi Au-Sb deposit

Py2–5 pyrite  $\delta^{34}\text{S}$  values in the ore stage varied from  $-5\text{‰}$  to  $5\text{‰}$  and more than 80% of the data were concentrated in a range of  $-3\text{‰}$ – $3\text{‰}$ ; however, differences during the different stages corresponded with the observed

Mineralizing periods Minerals	Pre-metallogenic	Metallogenic epoche			Late-metallogenic
		I	II	III	
Arsenopyrite		Apy1	Apy2		Apy3
Pyrite	Py1	Py2+3	Py4+5		Py6+7
Stibnite					
Skinnerite					
Bournonite					
Valentinite					
Quartz					
Calcite					

**Fig. 6** Mineral paragenetic association and formation sequence of the Baidi Au-Sb deposit

multi-zoned microscopic characteristics of the minerals and the varying characteristics of multiple bands. The  $\delta^{34}\text{S}$  values ore in the post-ore stage were concentrated at  $-5$ – $0$  ‰, which were highly coincident with some data from the stage; however, the overall values were low and mainly negative.

According to the formation characteristics of the minerals, Apy1 and Apy2 formed with pyrite during ore age, as Apy1 was closely associated with Py2 and Py3, and their  $\delta^{34}\text{S}$  values were similar and concentrated near zero and positive values. Apy2 formed in quartz veins, and its  $\delta^{34}\text{S}$  values were consistent with those of Apy1. Except for a few values, the values were positive and overall larger than those of Apy1, which is consistent with the  $\delta^{34}\text{S}$  values of the associated pyrite. This similarity explains the consistency of the sulfur source and the paragenetic characteristics. The Apy3 associated with pyrite in carbonate veins still had  $\delta^{34}\text{S}$  values in the range of  $-5$ – $5$  ‰, but were higher than those of the associated pyrite. Therefore, the arsenopyrite  $\delta^{34}\text{S}$  values from any stage were higher than those of pyrite in the same stage, and the arsenopyrite was more enriched in  $^{34}\text{S}$  (Table 2 and Fig. 7).

The  $\delta^{34}\text{S}$  values of the late stibnite were similar to those of the late pyrite (average of  $-5.6$  ‰). Compared with the above minerals, the stibnite  $\delta^{34}\text{S}$  values were the lowest, which is consistent with the thermodynamic fractionation characteristics of  $^{34}\text{S}$  enrichment and depletion owing to differences in mineral types associated with sulfur deposition (Ohmoto 1972; Shan et al. 2009) (Table 2 and Fig. 7). It is speculated that the source of sulfur for the stibnite should be consistent with those of the arsenopyrite and pyrite; however, the addition of sedimentary (reduced) sulfur may occur simultaneously.

During the ore stage, the pyrite and arsenopyrite had high contents of Au, As, and other elements; thus, the ore stage (Py2–5 and  $\delta^{34}\text{S}$  values of Apy1–Apy2) was most representative of the ore-forming fluid, with  $\delta^{34}\text{S}$  values ranging from  $-5$  ‰ to  $5$  ‰. Therefore, we inferred that the sulfur source may have been deep magmatic hydrothermal fluids or homogenized sedimentary strata (Ohmoto 1972; Ohmoto and Rye 1979). The source characteristics of the Ceheng area, which includes the Baidi Au-Sb deposit, have been inferred from the rare earth elemental contents of the clastic rocks. Both Co/Th-La/Sc and La/Th-Hf values reflect a felsic source (Chen et al. 2020). The rock body located nearest ( $\sim 100$  km) to the Baidi deposit is a felsic vein on the southeastern side (Fig. 1), with an age of 91–95 Ma (Maohong et al. 2011; Chen et al. 2015). Fission track ages of quartz in the Baidi deposit's ore period range from  $85.5 \pm 6.8$  to  $90.8 \pm 6.4$  Ma (Zhang and Yang 1992); therefore, we inferred that the deep part of the Baidi deposit was supplied by a rock mass with likely felsic attributes.

## 6.2 Formation of major sulfides

According to the Au contents of the sulfides, the main Au-bearing sulfides in the Baidi Au-Sb deposit are arsenopyrite and pyrite. According to their compositions, both are double sulfides, in which S, As, and Sb form anion pairs with covalent bonds, which combine with Fe to precipitate pyrite or arsenopyrite.

Previous studies have shown that a small range of water-rock interaction surfaces at the bottom of the basin were anoxic owing to the influence of sulfate-reducing bacteria or other biological activity, thereby allowing Fe sulfides to form (Ohmoto and Rye 1979; Schieber 2002; Scholz and Neumann 2007). The sulfides formed in this environment are relatively enriched in some trace elements, including Cu, Cd, V, Cr, Co, As, Ni, and Pb (Large et al. 2009; Xie et al. 2018; Yang et al. 2022). The positive correlation between Au and As ( $R^2 = 0.92$ ) during the ore stage was relatively high (Fig. 8). During this stage, fluid viscosity was high, minerals crystallized relatively quickly, and fine-grained strawberry-shaped Py1 formed easily (Butler and Rickard 2000). The structural and compositional characteristics of the pyrite formed during this stage were consistent with those obtained this study. This mineralization occurred parallel to the bedding plane (Fig. 4A, B) (Table 1).

During the mineralization stage (Py2–5 and Apy1–2), the pyrite exhibited large granular euhedral-hypidiomorphic structures (Fig. 4D and E) and obvious multi-zoning, indicating that the fluid was not injected continuously, but was injected in pulses. Unlike other typical Carlin-type Au deposits in southwest Guizhou Province (Jin and Li 2017; Xie et al. 2018; Chen et al. 2021), the Co/Ni ratio of the Baidi pyrite was  $< 1$  (Online Appendix 1), which may

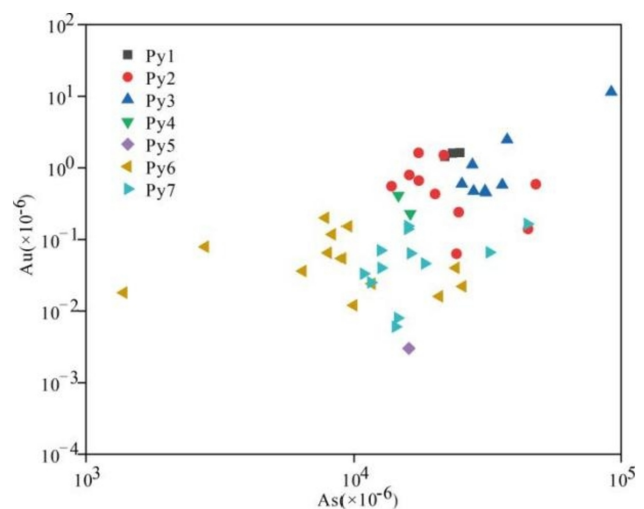


**Fig. 8** Diagram of the relationship between As and Au contents in pyrite

have been the result of sedimentary genesis after metamorphism and transformation. Compared with Py1, the pyrite in the mineralization stage was mostly distributed in sandstones, siltstones, and quartz veins as granular and aggregate blocks with relatively constant Au contents. Although the Py3 Au content during the mineralization stage was 11 ppm, the other samples had values similar to or lower than those of Py1. The trace elemental contents of V, Cr, Co, and Ni decreased significantly in the ore stage, whereas those of Cu, Zn, As, Sb, Pb, and Bi increased significantly (Fig. 9). The average As content in the mineralization stage was 29,235 ppm and reached a 91,910 ppm maximum. The Au content was the highest, and its overall correlation with the As content in the mineralization period was 0.791 (Fig. 8). According to the solubility of Au in As-bearing pyrite, the Au:As ratio is less than 0.02 ( $C_{Au} = 0.02C_{As} + 4 \times 10^{-5}$ ) and Au is likely to exist as lattice Au (Reich et al. 2005).

In addition, a considerable amount of Au-bearing arsenopyrite formed, most of which was distributed in sandstones, mudstones, quartz veins, and carbonate veins

as needle-shaped, lance-shaped, and radial aggregates. A few were also encased in stibnite and exhibited higher Au contents (average > 80 ppm) than those of pyrite, indicating that arsenopyrite is the main Au-bearing mineral in the Baidi deposit. Based on its paragenetic association with pyrite, arsenopyrite was mostly arranged radially at the edges of the pyrite (Figs. 3C, 4B, and 4D), and formed later than some pyrite, which is consistent with observed sequences among Au-bearing minerals in Carlin-type Au deposits (Ohmoto and Rye 1979; Chen et al. 2009). Moreover, the Baidi pyrite had high As contents (average of 21070 ppm, maximum of 91910 ppm), suggesting that the As content of the ore-forming fluid was generally high, which would provide favorable conditions for arsenopyrite formation. Previous studies of Au in Baidi arsenopyrite (Hu et al. 2001; Li et al. 2002; Chen et al. 2009) have shown that its As and S contents are notably higher than that of Fe from Apy1 to Apy2 during the mineralization stage. Therefore, we speculate that Au substitutes into the Fe position, which may be  $Fe^{3+}$  or excess  $As^{3+}$  (Johan et al. 1989). In addition, the Au content of the same

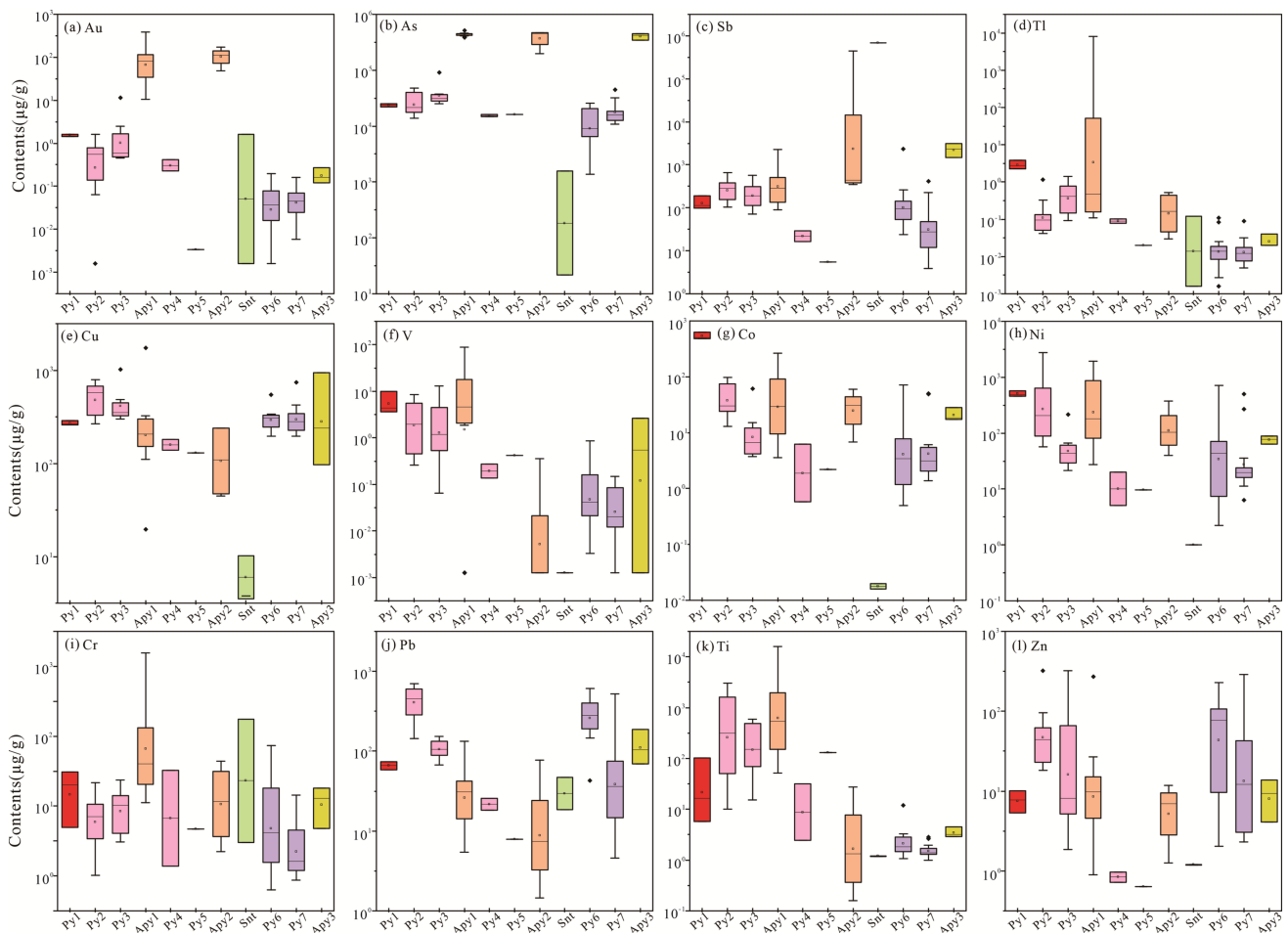


**Fig. 9** Box plots of Au, As, Cu, Pb, Tl, Sb, Co, Ni, Cr, V, Ti, and Zn content variations

arsenopyrite particle could have different values, which may result from the instability of the Fe valence state, thereby leading to the substitution instability of  $\text{Au}^{3+}$ . However, it is possible that the multi-stage nature of the fluid injection caused changes in the As content. In addition, although we obtained a positive correlation between high As and Au contents in this study, this range was not significant for pyrite. The Au content of the pyrite was not high, and in most cases it was less than the Au content of the arsenopyrite. Pyrite was also more enriched in  $^{32}\text{S}$ , whereas arsenopyrite was more enriched in  $^{34}\text{S}$ . Both of these minerals are fractionated and paragenetic.

The Sb ore exists as euhedral schistose stibnite in quartz veins, which developed later than the Au mineralization stage. The abundance of Sb was low in all spheres. During the Au mineralization stage, the Sb content was enriched to a certain extent but was mostly concentrated at 1000 ppm (Fig. 9), which is insufficient to form stibnite in later stages. Therefore, the Sb source was not only deep magmatic hydrothermal fluids inferred from the  $\delta^{34}\text{S}$  value. Sb in clastic rocks (Zhang et al. 2020) may have been extracted under the action of magmatic hydrothermal fluid flow. The influence of regional deep and large faults then caused precipitation along the extensional zones of faults or in regions with obvious steep and gentle changes in dip (Fig. 2). This may explain why the stibnite  $\delta^{34}\text{S}$  value was less than  $-5\%$ , which is outside the range of mantle sulfur and manifests as sedimentary (reduced) sulfur.

The fluid evolution can be determined from the trace elemental contents of the Baidi Au-Sb deposit (Fig. 9). Initially, sedimentary strawberry Py1 formed, which has elemental contents representative of the sedimentary strata. Owing to the pulsed fluid flow, the elemental contents of the main Au-bearing minerals (Py2–5 and Apy1–2) differed or increased/decreased. However, during the Sb mineralization stage and later stages without ore (Py6–7 and Apy3), the elemental contents were similar to those of the sedimentary strata, which is consistent with the sulfur isotope results and explains the mixing of deep fluids with sedimentary fluids in the later stage. These conditions are necessary for Au and Sb paragenesis. First, the pulsed injections of deep fluids provided ore-forming materials, particularly Au. Second, the fluid extracted elements from the formation (i.e., Sb). Thus, under strong tectonic action, the Sb-bearing minerals precipitated in extensional areas in the late stage. Therefore, determining the role of the regional structure in the formation of the Baidi deposit should be a focus of future study.

### 6.3 Metallogenesis of the Baidi Au–Sb deposit

After the above discussion, we can summarize the general process of the formation of Baidi gold-antimony deposit

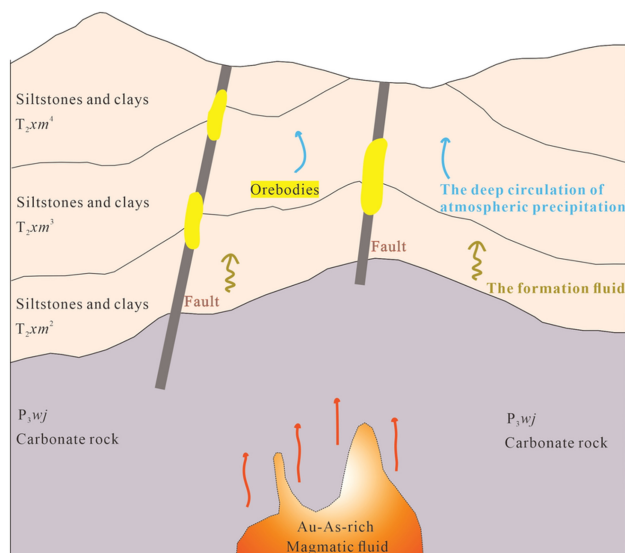


**Fig. 10** Metallogenesis model for the Baidi Au-Sb deposit

(Fig. 10). The main metallogenic period began in the late Yanshanian, and the fluid carrying the main ore-forming element Au moved upward along the extensional faults (Chen et al. 2021; Zhang and Yang 1992), these fluids formed the initial form of the Baidi gold-antimony deposit, characterized by high Au, As, low to moderate salinity (3.33% ~ 6.59% NaCl eqv.), temperature (177 ~ 250 °C), and acidity (3.6 ~ 3.9) (Ji et al. 2018). Subsequently, in the process of migration, more abundant Sb is extracted from the deep circulation of atmospheric precipitation and formation fluid (Zhang et al. 2020), and finally Au and Sb are unloaded by water–rock reaction in the zone with obvious occurrence change at the intersection of anticlines and faults, thus converging Au–Sb paragenetic deposits.

## 7 Conclusions

The main Au-bearing minerals in the Baidi Au-Sb deposit are arsenopyrite and pyrite. Arsenopyrite can be divided into mineralization (Apy1–2) and post-mineralization (Apy3) stages, which can be further divided into pre-mineralization (Py1), mineralization (Py2–5), and post-mineralization (Py6–7) stages. The main Sb-bearing mineral was stibnite, with some skinnerite, bournonite, and valentinite.

The Au- and Sb-bearing minerals in the Baidi deposit formed in order of Py1, Py2–3 + Apy1, Py4–5 + Apy2, Py6–7 + Apy3, and Snt. The Au and sulfur isotopic contents of the arsenopyrite were higher than those of pyrite in all stages. We speculate that Au is more easily enriched in arsenopyrite containing heavy sulfur in the Baidi Au-Sb deposit.

The sulfur isotopic values of the paragenetic arsenopyrite and pyrite were relatively consistent, all of which ranged from  $-5$  to  $5\text{‰}$  and were concentrated in the range of  $-3$ – $3\text{‰}$ , which corresponds to sulfur derived from deep magmatic hydrothermal fluids or from homogenized sedimentary strata. Combined with the stibnite sulfur isotopic characteristics ( $< -5\text{‰}$ ) in the later stage period, these results indicate that the presence of sulfur in the Baidi Au-Sb deposit is the result of contributions from sedimentary sulfur. In addition, changes in the trace elemental contents confirm that the Baidi Au-Sb deposit underwent pulsed hydrothermal mineralization and eventually returned to a sedimentary source. Therefore, we presume that the sulfur source may have been deep magmatic hydrothermal fluids, with added sedimentary sulfur in the later stage.

**Supplementary Information** The online version contains supplementary material available at <https://doi.org/10.1007/s11631-023-00653-3>.

**Acknowledgements** We wish to thank No.117 Geological Team, Guizhou Bureau of Geology and Mineral Exploration and Development for help during our field investigation.

**Author contributions** Conceptualization, QT and YX; methodology, JY; software, JY and QT; validation, QT, YX and ZX; formal analysis, JY and QT; collected samples, JY, QT, YX, ZX and GJ; drawn the geologic maps, JY, QT, ZX and GJ.

**Funding** This research was funded by the Science and Technology Foundation of Guizhou Province ([2019]1138, Qiankehezhicheng [2021] YiBan 403 and Qiankehepingtairencai-CXTD [2021] 007) and the Project for the Growth of Young Scientific and Technological Talents in Colleges and Universities of Guizhou Province ([2022]356). We wish to thank No.117 Geological Team, Guizhou Bureau of Geology and Mineral Exploration and Development for help during our field investigation.

**Data availability** Not applicable.

**Declarations**

**Conflict of interest** The authors declare no conflict of interest.

## References

- Butler IB, Rickard D (2000) Framboidal pyrite formation via the oxidation of iron (II) monosulfide by hydrogen sulphide. *Geochim Cosmochim Acta* 64:2665–2672
- Chen MH, Mao JW, Chen ZY, Zhang W (2009) Mineralogy of arsenian pyrites and arsenopyrites of Carlin-type gold deposits in Yunnan-Guizhou-Guangxi golden triangle area, southwestern China. *Min Depos* 28:539–557
- Chen MH, Mao JW, Li C, Zhang ZQ, Dang Y (2015) Re–Os isochron ages for arsenopyrite from Carlin-like gold deposits in the Yunnan–Guizhou–Guangxi “golden triangle”, southwestern China. *Ore Geol Rev* 64:316–327
- Chen X, Peng CL, Chen JS, Wu KB, Zhang DM (2020) Geochemistry and provenance of the Middle Triassic clastic rocks in the Youjiang Basin, Ceheng, Guizhou. *Geol J China Univ* 26:639–655
- Chen J, Huang ZL, Yang RD, Du LJ, Liao MY (2021) Gold and antimony metallogenic relations and ore-forming process of Qinglong Sb(Au) deposit in Youjiang basin, SW China: sulfide trace elements and sulfur isotopes. *Geosci Front* 12:605–623
- Chen HD, Zeng YF (1990) Nature and evolution of the Youjiang Basin. *Sediment Facies Palaeogeogr* 28–37
- Du YS, Huang H, Yang JH, Huang HW (2013) The Basin translation from Late Paleozoic to Triassic of the Youjiang Basin and its tectonic signification. *Geol Rev* 59:1–11
- Fang C, Ji GS, Wu DY, Wu ZJ, Xian K, Zhang ZH (2013) Discussion on geology feature and prospecting direction of Baidi gold deposit in Ceheng county of Guizhou province, China. *Acta Mineral Sin* 33:308–314
- Guo ZC (1988) The geological features and origin of the Zimudang gold deposit in Xingren County, Guizhou province. *Guizhou Geol* 5:201–218+295
- Hofstra AH, Cline JS (2000) Characteristics and models for Carlin-type gold deposits. *Rev Econ Geol* 163–220
- Hou L, Peng HJ, Ding J, Zhang JR, Zhu SB, Wu SY, Wu Y, Ouyang HG (2016) Textures and in situ chemical and isotopic analyses of pyrite, Huijiabao trend, Youjiang basin, China: implications for paragenesis and source of sulfur. *Econ Geol* 111:331–353
- Hu WX, Zhang WL, Hu SX, Hua RM, Zhu JM (2001) Determination of structural gold in Au-bearing arsenopyrite and its formation mechanism. *Acta Geosci Sin* 75:410–418
- Hu RZ, Su WC, Bi XW, Tu GZ, Hofstra AH (2002) Geology and geochemistry of Carlin-type gold deposits in China. *Miner Depos* 37:378–392
- Hu RZ, Fu SL, Xiao JF (2016) Major scientific problems on low-temperature metallogenesis in South China. *Acta Petrol Sin* 32:3239–3251
- Ji GS (2014) Geochemical characteristics and its genesis of Baidi gold deposit in Ceheng of Guizhou. *Guizhou Geol* 31:21–26
- Ji GS, Wu ZJ, Peng CG, Lu JB, Zhang ZH, Chen ZS, Liu H (2018) Preliminary research on prospecting model of Baidi gold deposit in Ceheng county of south west Guizhou. *Min Resour Geol* 32:465–473
- Jian P, Liu D, Kröner A, Zhang Q, Wang YZ, Sun XM, Zhang W (2009) Devonian to Permian plate tectonic cycle of the Paleoe-Tethys Orogen in southwest China (II): insights from zircon ages of ophiolites, arc/back-arc assemblages and within-plate igneous rocks and generation of the Emeishan CFB province. *Lithos* 113:767–784
- Jin XY, Li JW (2017) Geology, mineralization and genesis of the Nibao, Shuiyindong and Yata gold deposits in SW Guizhou Province, China. Doctor, China University of Geosciences
- Johan Z, Marcoux E, Bonnemaïson M (1989) A arsenopyrite aurifère: Mode de substitution de Au dans la structure de FeAsS. *Academic decience(Paris) Comptes Rendus* 185–191 (in French)
- Large RR, Danyushevsky L, Hollit C, Maslennikov V, Meffre S, Gilbert S, Bull S, Scott R, Emsbo P, Thomas H, Singh B, Foster J (2009) Gold and trace element zonation in pyrite using a laser imaging technique: implications for the timing of gold in orogenic and carlin-style sediment-hosted deposits. *Econ Geol* 104:635–668
- Lehrmann DJ, Enos P, Payne JL, Montgomery P, Wei JY, Yu YY, Xiao JF, Orchard MJ (1978) Permian and Triassic depositional history of the Yangtze platform and Great Bank of Guizhou in the Nanpanjiang basin of Guizhou and Guangxi, south China. *Res Gate* 33:149–168

- Li ZQ, Chen SD, Wang JZ, Li FC (1995) Isotope geochemistry of Jinya disseminated gold deposit in western Guangxi. *Min Petrol* 15:66–72
- Li JL, Qi F, Xu QS (2002) A further study on the chemical state of “Combined gold” in minerals of negative valence gold-arsenopyrite and arseniferous pyrite. *Prog Nat Sci* 12:952–958
- Li CY (1999) Some geological characteristics of concentrated distribution area of epithermal deposits in China. *Earth Sci Front* 6:164–171
- Liu Y, Hu Z, Gao S, Günther D, Xu J, Gao CG, Chen HH (2008) In situ analysis of major and trace elements of anhydrous minerals by LA-ICP-MS without applying an internal standard. *Chem Geol* 257:34–43
- Liu P, Li PG, Li KQ, Lei ZY, Li XH, Song WH, Zhang HS (2006) The elementary analysis about mineralization geological process of gold deposit in south west Guizhou. *Guizhou Geol* 23:83–87+90–92+97
- Maohong C, Jingwen M, Bierlein FP, Norman T, Uttley PJ (2011) Structural features and metallogenesis of the Carlin-type Jinfeng (Lannigou) gold deposit, Guizhou Province, China. *Ore Geol Rev* 43:217–234
- Metcalf I (2013) Gondwana dispersion and Asian accretion: tectonic and palaeogeographic evolution of eastern Tethys. *J Asian Earth Sci* 66:1–33
- Ohmoto H (1972) Systematics of sulfur and carbon isotopes in hydrothermal ore deposits. *Econ Geol* 67:551–578
- Ohmoto H, Rye RO (1979) *Isotopes of sulfur and carbon, geochemistry of hydrothermal ore deposits*, 2nd edn. Wiley, New York
- Pearce NJG, Perkins WT, Westgate JA, Gorton MP, Jackson SE, Neal CR, Chenery SP (1997) A compilation of new and published major and trace element data for NIST SRM 610 and NIST SRM 612 glass reference materials. *Geostand Geoanal Res* 21:115–144
- Qi JY (2006) *Modern analysis and testing technology*. Tongji University Press, Shanghai
- Qiu L, Yan DP, Tang SL, Wang Q, Yang WX, Tang XL, Wang JB (2016) Mesozoic geology of southwestern China: Indosinian foreland overthrusting and subsequent deformation. *J Asian Earth Sci* 122:91–105
- Reich M, Kesler SE, Utsunomiya S, Palenik CS, Chryssoulis SL, Ewing RC (2005) Solubility of gold in arsenian pyrite. *Geochim Cosmochim Acta* 11:2781–2796
- Schieber J (2002) Sedimentary pyrite: a window into the microbial past. *Geology* 30:531
- Scholz F, Neumann T (2007) Trace element diagenesis in pyrite-rich sediments of the Achterwasser lagoon, SW Baltic Sea. *Mar Chem* 107:516–532
- Shan L, Zheng YY, Xu RK, Cao L, Zhang YL, Lian YJ, Li YH (2009) Review on sulfur isotopic tracing and hydrothermal metallogenesis. *Geol Resour* 18:197–203
- Su WC, Dong WD, Zhang XC, Shen NP, Hu RZ, Hofstra AL, Cheng LZ, Xia Y, and Yang KY (2018) Carlin-style gold deposits in the Dian-Qian-Gui “golden triangle” of southwest China *Reviews in Economic Geology* 20:157–185
- Tan QP, Xia Y, Xie ZJ, Yan J, Wei DT (2015) S, C, O, H, and Pb isotopic studies for the Shuiyindong Carlin-type gold deposit, Southwest Guizhou, China: constraints for ore genesis. *Chin J Geochem* 34:525–539
- Tu GC (2002) Two unique mineralization areas in Southwest China. *Bull Mineral Petrol Geochem* 21:1–2
- Wang X, Metcalfe I, Jian P, He LQ, Wang CS (2000) The Jinshajiang-Ailaoshan suture zone, China: tectonostratigraphy, age and evolution. *J Asian Earth Sci* 18:675–690
- Wu ZJ, Ji GS, Zhang ZH, Zhao MF, Chen ZS (2020) Geochemical characteristics of trace elements in Baidi gold deposit, Ceheng county, Guizhou province. *Modern Min* 36:30–33
- Xia Y (2005) Characteristics and model for Shuiyindong Au deposit in southwestern Guizhou, China. PhD dissertation, Guiyang, China, Institute of Geochemistry, Chinese Academy of Sciences
- Xie Z, Xia Y, Cline JS, Pribil MJ, Koenig A, Tan QP, Wei DT, Wang ZP, Yan J (2018) Magmatic origin for sediment-hosted Au deposits, Guizhou Province, China. In-situ chemistry and sulfur isotope composition of pyrites Shuiyindong and Jinfeng deposits. *Econ Geol* 113:1627–1652
- Xu JH (1987) Some problems of geotectonics in South China. *Bull Geol Sci Technol* 6:13–27
- Yan J, Hu R, Liu S, Lin YT, Zhang JC, Fu SL (2018) NanoSIMS element mapping and sulfur isotope analysis of Au-bearing pyrite from Lannigou Carlin-type Au deposit in SW China: new insights into the origin and evolution of Au-bearing fluids. *Ore Geol Rev* 92:29–41
- Yang CF, Liu JZ, Gu XX, Wang ZP (2020) The relationship of tectonic evolution and Au-Sb Mineralization in Nanpanjiang-Youjiang Basin. *Acta Geosci Sin* 41:280–292
- Yang L, Wang Q, Large RR, Fougereuse D, Mukherjee I, Zhang QZ, Deng J (2022) Texture and geochemistry of pyrite from the Jinya, Nakuang and Gaolong gold deposits in the Youjiang Basin: implications for basin-scale gold mineralization. *Miner Depos* 57:1367–1390
- Yin HF, Wu SB, Du YS, Peng YQ (1999) South China defined as part of tethyan archipelagic ocean system. *Earth Sci-J China Univ Geosci* 24:3–14
- Zhang YZ, Li H, Liu WH, Xu WX, Dai TG (2008) Isotope geochemistry of the Gaolong micro-disseminated gold deposit in Guangxi. *Acta Geosci Sin* 29:697–702
- Zhang Y, Xia Y, Wang ZP, Yan BW, Fu ZK, Chen M (2010) REE and stable isotope geochemical characteristics of Bojitian gold deposit, Guizhou province. *Earth Sci Front* 17:385–395
- Zhang TY, Li CY, Sun SJ, Hao XL (2020) Geochemical characteristics of antimony and genesis of antimony deposits in South China. *Acta Petrol Sin* 36:44–54
- Zhang F, Yang KY (1992) Fission track metallogenic epoch of fine disseminated gold deposits in southwestern Guizhou. *Chin Sci Bull* 1593–1595
- Zhou YZ, Hu RZ (1995) Research and development of low temperature geochemistry. *Adv Earth Sci* 10:442–444
- Zhu GR (2009) Structural character and formation mechanism of Baidi gold deposit in Ceheng, Guizhou. *Guizhou Geol* 26:177–179+184
- Zhuang XG (1995) The paleogeothermal field of northwestern Guangxi: characteristics and its role in the formation of micro-disseminated gold deposits. *Mineral Depos* 14:82–89

Springer Nature or its licensor (e.g. a society or other partner) holds exclusive rights to this article under a publishing agreement with the author(s) or other rightsholder(s); author self-archiving of the accepted manuscript version of this article is solely governed by the terms of such publishing agreement and applicable law.